


Article

Pt Nanowire-Anchored Dodecahedral $\text{Ag}_3\text{PO}_4\{110\}$ Constructed for Significant Enhancement of Photocatalytic Activity and Anti-Photocorrosion Properties: Spatial Separation of Charge Carriers and Photogenerated Electron Utilization

Hanxu Zhu ¹, Yekun Ji ¹, Lifang Chen ², Weilin Bian ²  and Jinnan Wang ^{1,*}

¹ State Key Laboratory of Pollution Control and Resource Reuse & School of the Environment Nanjing University, Nanjing 210023, China; hanxuzhunju@163.com (H.Z.); yekun_ji@163.com (Y.J.)

² Institute of Water Environmental Engineering & Technology, YanCheng 224000, China; li-fang-chen@163.com (L.C.); bianweilin1987@163.com (W.B.)

* Correspondence: wjnnju@163.com

Received: 24 December 2019; Accepted: 23 January 2020; Published: 8 February 2020



Abstract: Pt nanowire-anchored dodecahedral $\text{Ag}_3\text{PO}_4\{110\}$ was constructed for organics photodegradation. SEM and TEM images confirmed that the Pt nanowires were grafted on dodecahedral Ag_3PO_4 , which was entirely bounded by $\{110\}$ facets. All the X-ray diffraction peaks of the samples were indexed to the body-centered cubic phase of Ag_3PO_4 , indicating that Pt nanowire-anchored dodecahedral Ag_3PO_4 well maintained the original crystal structure. The rhombic dodecahedral Ag_3PO_4 entirely bounded by $\{110\}$ facets achieved high photocatalytic activity. Due to the formation of a Schottky barrier, the Pt nanowires improved the separation of the charge carriers of Ag_3PO_4 . Furthermore, they provided a fast expressway to transfer the photogenerated electrons and prolonged the lifetime of the charge carriers via long-distance transport, resulting in the accumulation of holes on Ag_3PO_4 for organics degradation. More importantly, the Pt nanowires improved the reduction potential of the photogenerated electrons for O_2 reduction to $\cdot\text{O}_2^-$, which enhanced the photocatalytic activity and anti-photocorrosion properties of Ag_3PO_4 . We found that 99.5% of Rhodamine B (RhB) could be removed over 0.5wt% Pt nanowire-anchored dodecahedral Ag_3PO_4 within 10 min. Even after 10 cycles, the photocatalytic activity was still high. photoluminescence (PL), time-resolved photoluminescence (TRPL), UV-vis diffuse reflectance spectra (UV-visDRS), and photoelectrochemical analysis showed that Pt nanowire-anchored dodecahedral Ag_3PO_4 exhibited lower bandgap, higher photocurrent intensity, better electronic conductivity, and longer charge carriers lifetime than other types of Ag_3PO_4 crystals. Radical trapping experiments and electron paramagnetic resonance (EPR) analysis demonstrated that the holes were the main active species for organics photodegradation.

Keywords: Pt nanowire-anchored dodecahedral $\text{Ag}_3\text{PO}_4\{110\}$; anti-photocorrosion; spatial charge carriers' separation; photogenerated electron utilization; oxygen reduction

1. Introduction

Ag_3PO_4 has been considered as the most potential visible-light photocatalyst due to its high quantum efficiency (90%, >420 nm) and positive valence band (VB = +2.9 eV) [1,2]. However, since the properties of catalyst are linked to their crystal facet-dependent surface atomic structure [3,4], the quantum efficiency of Ag_3PO_4 depends on its crystal facets [5,6]. Furthermore, different

morphologies of Ag_3PO_4 produced by self-assembly, such as porous microcubes [7], nanorods [8], tetrapods [9], dendritic nanostructures [10], concave trisoctahedral [11], could also influence the photocatalytic performance. In general, exposure of high-energy crystal facets can improve the photocatalytic activity. Ye et al. demonstrated that Ag_3PO_4 with {110} facets exhibited much higher photocatalytic activity for organics degradation than that Ag_3PO_4 with {100} facets [5]. Our previous work also indicated that 3D core-shell CQDs(carbon quantum dots)/ Ag_3PO_4 @benzoxazine tetrapod with exposure of more {110} facets could achieve higher visible-light photocatalytic activity and anti-photocorrosion [12]. However, most of the Ag_3PO_4 -based crystals were polycrystals bounded by different facets, which resulted in partial exposure of the {110} facets. In contrast to polycrystals, monocrystals could be entirely bounded by the same facets; therefore, monocrystalline Ag_3PO_4 might entirely expose its {110} facets. For this reason, monocrystal Ag_3PO_4 -based photocatalysts are expected to have significantly improved photocatalytic activity.

On the other hand, although the absolute exposure of high-energy facets of Ag_3PO_4 could improve the quantum efficiency, the photo-generated electrons of Ag_3PO_4 would preferably reduce Ag^+ to Ag^0 [$\text{Ag}^+ + e^- \rightarrow \text{Ag}^0$, +0.75 V vs. NHE(normal hydrogen electrode)] in the absence of scavengers, resulting in serious photocorrosion [2]. In order to improve the photocatalytic stability of Ag_3PO_4 , heterojunctions ($\text{Ag}_3\text{PO}_4/\text{Ti}_3\text{C}_2$ [13], $\text{Ag}_3\text{PO}_4/\text{SnSe}_2$ [14], $\text{Ag}_3\text{PO}_4/\text{Co}_3\text{O}_4$ [15]) and Z-schemes ($\text{Ag}_3\text{PO}_4/\text{CuBi}_2\text{O}_4$ [16], $\text{Ag}_3\text{PO}_4/g\text{-C}_3\text{N}_4$ [17], $\text{SrTiO}_3/\text{Ag}/\text{Ag}_3\text{PO}_4$ [18]) were constructed to improve charge separation. Our previous study also prepared $\text{TiO}_2@\text{MoS}_2/\text{Ag}_3\text{PO}_4$ to improve the anti-photocorrosion and photocatalytic activity [19]. Nevertheless, the construction of heterojunctions and Z-schemes required specific band positions of the dual semiconductors, which limited the fabrication of semiconductor composites [20,21]. Thus, the loading of noble metals on semiconductors appears a more facile and efficient method for the enhancement of charge separation. Due to the formation of a Schottky barrier with the semiconductor, various co-catalysts (Ag, Pt, Pd, and Au) could act as an electron sink for the improvement of the photogenerated charge separation [22,23]. By using time-correlated single-photon counting (TCSPC) spectroscopy, a slower fluorescence decay associated with the blocking of the electron recombination process was observed on ZnO/Au because of the formation of a Schottky barrier [24]. Our previous research also demonstrated that the co-catalyst Pd doped on GdCrO_3 could effectively delay the recombination of charge carriers due to the construction of an internal electric field [25]. Because of its higher work function (5.65 eV), Pt can more easily form a Schottky barrier with semiconductors than other noble metals. Thus, Pt has been considered as the most satisfying electron sink [26]. Moreover, the physical form of noble metals could obviously influence the conduction of a photogenerated charge [27–29]. Compared with 2D and 3D structures, a 1D nanostructure could not only provide a fast way to transfer the photogenerated electrons, but also prolong the lifetime of charge carriers [30]. Thus, loading noble metal nanowires on Ag_3PO_4 is expected to significantly improve the separation and transfer of the photogenerated charge.

Notably, these photogenerated electrons could promote anti-photocorrosion once transferred from Ag_3PO_4 to the co-catalysts surface. In the absence of a sacrificial agent, the photogenerated electrons of Ag_3PO_4 could be utilized by dissolved oxygen via a single-electron [$\text{O}_2 + e^- \rightarrow \text{O}_2^-$ (aqueous), -0.284 V, $\text{O}_2 + \text{H}^+ + e^- \rightarrow \text{HO}_2$, -0.046 V] or a multi-electron pathway [$\text{O}_2 + 2 \text{H}^+ + 2 e^- \rightarrow \text{H}_2\text{O}_2$ (aq), +0.682 V, $\text{O}_2 + 4 \text{H}^+ + 4 e^- \rightarrow 2 \text{H}_2\text{O}$, +1.23 V]. However, the rate of this reaction was very low or even negligible because of the positive conduction band(CB) of Ag_3PO_4 (+0.45 eV) [31]. Fortunately, the noble metal Pt could act as a co-catalyst, which not only promoted the transfer of the photogenerated charge via the formation of a Schottky barrier but also improved the reduction potential of photo-induced electrons by electron activation effects [32,33]. Many previous studies reported that Pt was the best catalyst for oxygen reduction reactions (ORR) because of the optimal oxygen-metal bond energy between the oxygen 2p states and the Pt d states [34,35]. Thus, it is expected that grafting 1D Pt nanowires into monocrystal Ag_3PO_4 {110} would simultaneously improve the transfer and the utilization of the photogenerated electrons.

Based on the above research background and assumptions, novel Pt nanowire-anchored dodecahedral $\text{Ag}_3\text{PO}_4\{110\}$ was constructed to improve the visible-light photocatalytic activity and anti-photocorrosion of the photocatalyst. Being entirely bounded by $\{110\}$ facets, rhombic dodecahedral Ag_3PO_4 achieved high photocatalytic activity. In addition, loading of 1D Pt nanowires on the rhombic dodecahedral Ag_3PO_4 could not only improve the charge carriers' separation but also provide a fast transfer of the photogenerated electrons in the axial direction, resulting in a longer lifetime of the charge carriers. On the other hand, the reduction potential of the photogenerated electrons was enhanced by Pt nanowires due to the formation of a Schottky barrier, which improved the utilization of the photogenerated electrons for oxygen reduction. Thus, Pt nanowire-anchored dodecahedral $\text{Ag}_3\text{PO}_4\{110\}$ exhibited excellent photocatalytic performance and anti-photocorrosion properties. The present work is focused on the following aspects: 1) construction and characterization of Pt nanowire-anchored dodecahedral $\text{Ag}_3\text{PO}_4\{110\}$, 2) evaluation of the photocatalytic activity and anti-photocorrosion ability of Pt nanowire-anchored dodecahedral $\text{Ag}_3\text{PO}_4\{110\}$, 3) description of the possible mechanisms of enhancement of the photocatalytic and anti-photocorrosion activities.

2. Results and Discussion

2.1. Structure and Composition

SEM images indicated that the morphology and crystal structure of Ag_3PO_4 were obviously influenced by the precursor used in the synthetic process. AgNO_3 used as a precursor can yield Ag_3PO_4 irregular spheres (Figure 1A). However, in the system of silver acetate/acetic acid, CH_3COO groups could facilitate the formation of high-energy facets $\{110\}$ in Ag_3PO_4 , promoting the crystal growth of uniform rhombic dodecahedrons (Figure 1B and Figure S1). In addition, ultrasonic exfoliation could break the Pt nanowire net (Figure 1C) into singular Pt nanowires (inset of Figure 1C and Figure S2). Such 1D Pt nanowires could be grafted on the rhombic dodecahedrons more uniformly (Figure 1E,F and Figure S3) than Pt nanoparticles (Figure 1D). The amine species on Pt nanowires' surface produced from the reaction of DMF and KOH [36] formed Ag-NH_3 bonds with rhombic dodecahedral Ag_3PO_4 , strengthening the combination of Ag_3PO_4 and Pt nanowires. Fourier-transform infrared spectroscopy (FT-IR) results confirmed the presence of amine groups (Figure S4).

X-ray diffraction (Figure 1G) indicated that all the diffraction peaks of the samples were indexed as body-centered cubic phase of Ag_3PO_4 (JCPDS No. 06-0505). Thus, the Pt nanowire-anchored dodecahedral $\text{Ag}_3\text{PO}_4\{110\}$ composite well maintained the origin crystal structure of Ag_3PO_4 . The diffraction peaks at 38.1° , 44.2° were ascribed to the $\{111\}$ facet and the $\{200\}$ facet of the Pt nanowires, respectively (JCPDS No. 87-0647) [37]. Notably, HR-TEM (Figure 1H) and the selected-area electron diffraction (SAED) pattern (Figure 1I) indicated high crystallinity of the single-crystal Pt nanowires with the $\{111\}$ facet. Thus, Pt nanowire-anchored dodecahedral $\text{Ag}_3\text{PO}_4\{110\}$ with exposure of high-energy facets was successfully fabricated.

As shown by X-ray photoelectron spectroscopy, characteristic 4f peaks of Pt could be clearly observed in the scanned spectra of Pt nanowire-anchored dodecahedral Ag_3PO_4 (Figure 2A), while they could not be identified in the spectra of pure dodecahedral Ag_3PO_4 . Furthermore, Pt 4f (Figure 2B) peaks could be deconvoluted into three distinctive doublet peaks, which were ascribed to the Pt $4f_{5/2}$ and $4f_{7/2}$ levels of Pt (0), Pt (II), Pt (IV). Notably, the characteristic peaks of Ag $3d_{3/2}$ (373.4 eV) and Ag $3d_{5/2}$ (367.4 eV) (Figure 2C and Figure S5) in Pt nanowire-anchored dodecahedral Ag_3PO_4 showed a slight shift compared with pure dodecahedral Ag_3PO_4 , which further confirmed the formation of Ag^+-NH_3 bonds. In addition, the peaks at 132.5 eV (Figure 2D), 530 eV, and 532 eV (Figure 2E) were respectively ascribed to P^{5+} and O^{2-} in Pt nanowire-anchored dodecahedral Ag_3PO_4 and to the adsorbed OH groups [38].

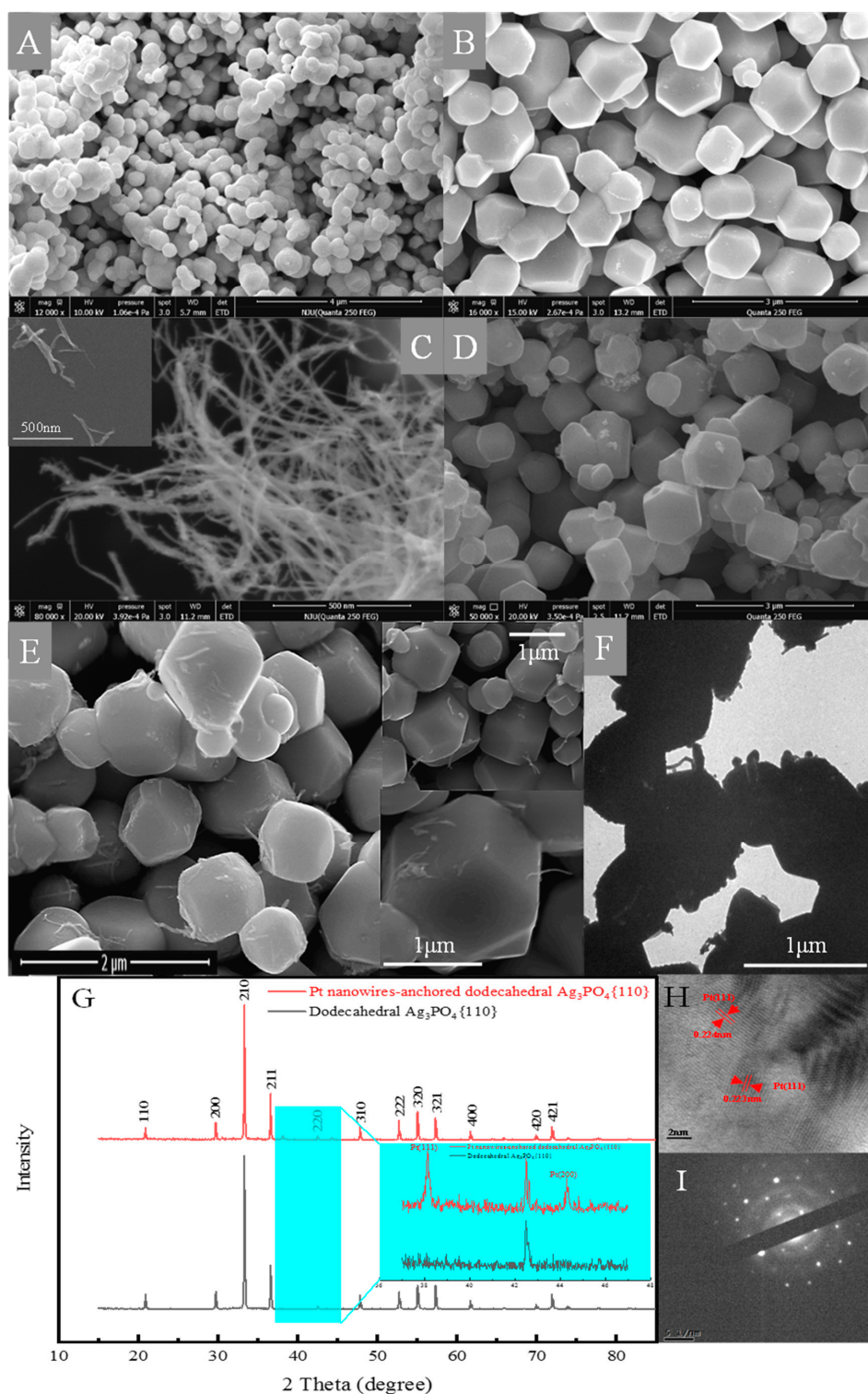


Figure 1. SEM images of synthesized (A) irregular spherical Ag₃PO₄, (B) rhombic dodecahedral Ag₃PO₄, (C) pure Pt nanowires, (D) Pt particles/dodecahedral Ag₃PO₄, (E) Pt nanowire-anchored dodecahedral Ag₃PO₄. (F) TEM image of Pt nanowire-anchored dodecahedral Ag₃PO₄, (G) XRD patterns of pure dodecahedral Ag₃PO₄ and of the Pt nanowire-anchored dodecahedral Ag₃PO₄ composite, (H) high-resolution (HR)-TEM image, and (I) selected-area electron diffraction (SAED) pattern of the Pt nanowires.

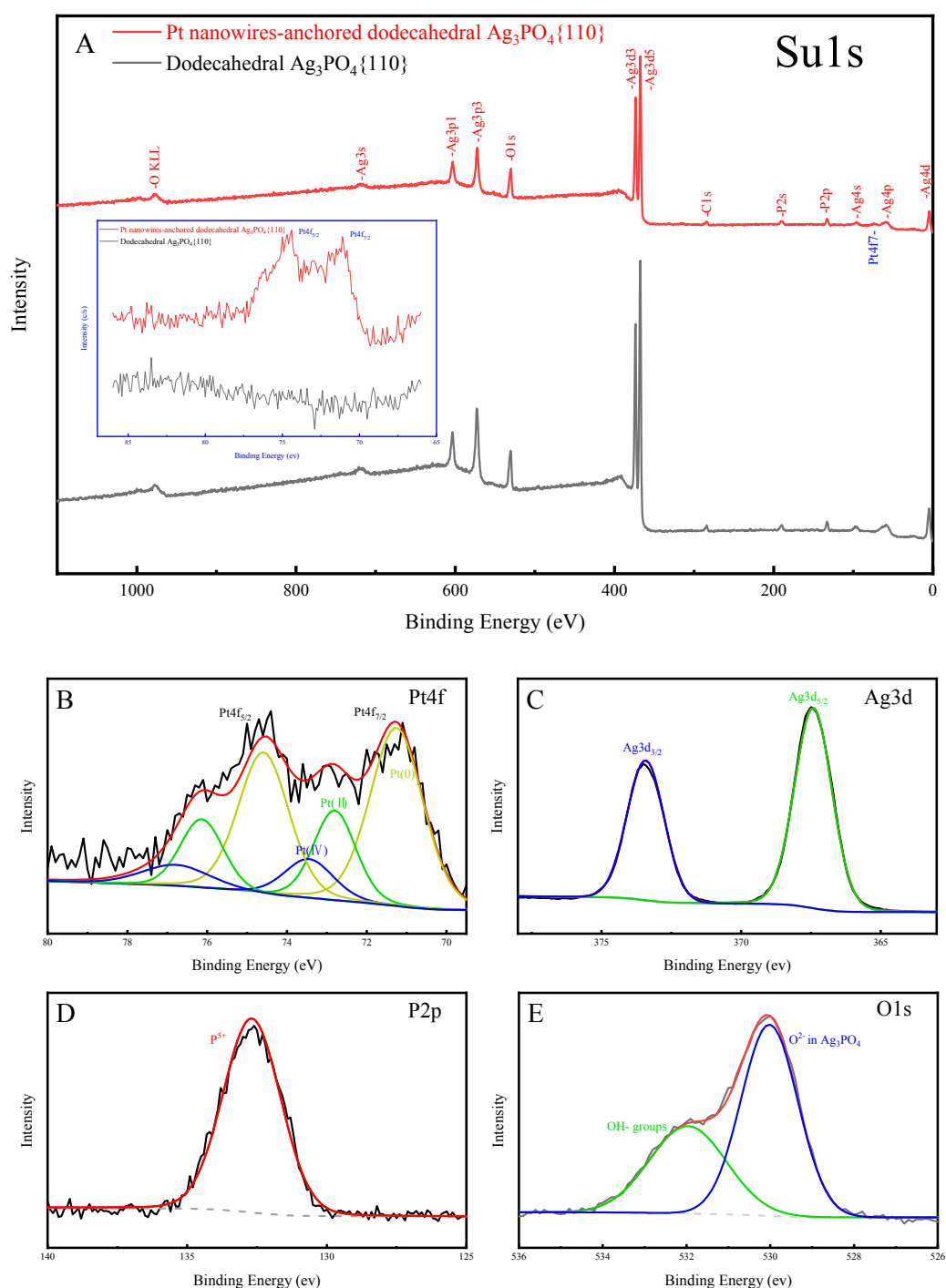


Figure 2. (A) Survey XPS spectra and high-resolution XPS spectra of Pt 4f (inset) in pure dodecahedral $\text{Ag}_3\text{PO}_4\{110\}$ and of the Pt nanowire-anchored dodecahedral $\text{Ag}_3\text{PO}_4\{110\}$ composite. High-resolution XPS spectra for (B) Ag 3d, (C) Pt 4f, (D) P 2p, (E) O 1s of Pt nanowire-anchored dodecahedral $\text{Ag}_3\text{PO}_4\{110\}$ composite.

2.2. Photoelectric Properties

UV-vis DRS analysis (Figure 3A) indicated that the optical absorption of dodecahedral $\text{Ag}_3\text{PO}_4\{110\}$ was much higher than that of Ag_3PO_4 irregular spheres. Furthermore, due to the difference of the carrier effective mass on different facets [6], the bandgap of dodecahedral $\text{Ag}_3\text{PO}_4\{110\}$ (2.35 eV) was lower than that of Ag_3PO_4 irregular spheres (2.42 eV). In addition, although loading of Pt nanowires

or Pt particles on dodecahedral $\text{Ag}_3\text{PO}_4\{110\}$ slightly decreased the optical absorption, the bandgap of the composite was not changed.

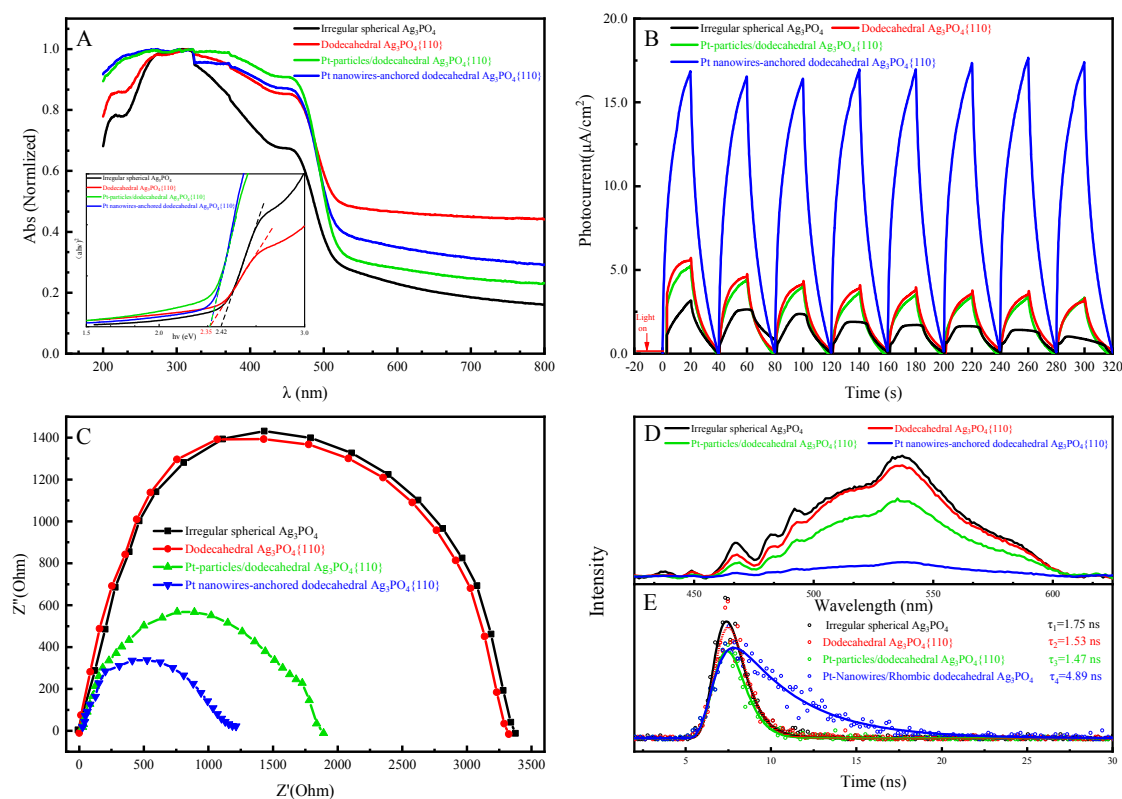


Figure 3. Photoelectric properties of different photocatalysts (A) UV-vis diffuse reflectance spectra (DRS) and the corresponding Kubelka–Munk transformed reflectance spectra (inset), (B) photocurrent response (Xe arc lamp, 350 W), (C) Electrochemical impedance spectroscopy (EIS) Nyquist plots, (D) photoluminescence (PL) and (E) time-resolved photoluminescence (TRPL) spectra.

The charge separation of different samples was evaluated by transient photocurrent response (Xe lamp, 350 W) (Figure 3B), resulting in the following order: Pt nanowire-anchored dodecahedral $\text{Ag}_3\text{PO}_4\{110\}$ > Pt particles/dodecahedral $\text{Ag}_3\text{PO}_4\{110\}$ > dodecahedral $\text{Ag}_3\text{PO}_4\{110\}$ > irregular spherical Ag_3PO_4 . As expected, Pt nanowire-anchored dodecahedral $\text{Ag}_3\text{PO}_4\{110\}$ exhibited the highest photocurrent intensity, which was six times higher than that of the Ag_3PO_4 irregular spheres. Since the electronic wavefunctions were constrained by quantum effects in nanoscale directions, 1D nanostructures could provide a fast transfer of the photogenerated electrons in the axial direction [30]. Thus, Pt nanowire-anchored dodecahedral $\text{Ag}_3\text{PO}_4\{110\}$ achieved a much higher photocurrent response than Pt particles/dodecahedral $\text{Ag}_3\text{PO}_4\{110\}$. Similarly, electrochemical impedance measurements (Figure 3C) indicated that the electronic conductivity of the photocatalysts was as follows: Pt nanowires-anchored dodecahedral $\text{Ag}_3\text{PO}_4\{110\}$ > Pt particles/dodecahedral $\text{Ag}_3\text{PO}_4\{110\}$ > dodecahedral $\text{Ag}_3\text{PO}_4\{110\}$ > irregular spherical Ag_3PO_4 . The EIS Nyquist plots of Pt nanowire-anchored dodecahedral Ag_3PO_4 showed the smallest arc radius, demonstrating that Pt nanowires loaded on Ag_3PO_4 dodecahedrons significantly accelerated interfacial electron transfer. Such improvement of photocurrent response and electronic conductivity confirmed the enhancement of charge carriers' separation and transfer of Pt nanowire-anchored dodecahedral Ag_3PO_4 .

In addition, the lowest recombination rate of photogenerated carriers was observed in the photoluminescence emission spectra of Pt nanowire-anchored dodecahedral Ag_3PO_4 (Figure 3D). This suggested that the photo-carriers could be effectively separated via the Schottky effect and then immediately transferred to the surface of Pt nanowires. Fluorescence decay curves, which

reflect the charge carriers' lifetime [39,40], are shown in the time-resolved photoluminescence spectra (Figure 3E). Compared with the other three samples ($\tau = 1.75$ ns, 1.53 ns, 1.47 ns), Pt nanowire-anchored dodecahedral Ag_3PO_4 displayed the longest fluorescence lifetime ($\tau = 4.89$ ns), which indicates that the loading of Pt nanowires can significantly prolong the charge carriers' lifetime of Ag_3PO_4 . Such decrease of photoluminescence intensity and prolongation of fluorescence lifetime might be attributed to the efficient charge carriers' separation and long-distance photogenerated electron transport and diffusion on 1D Pt nanowires.

2.3. Photocatalytic Activity and Anti-Photocorrosion

Due to the absolute exposure of the {110} facets, the Ag_3PO_4 rhombic dodecahedrons showed higher photocatalytic activity than the Ag_3PO_4 irregular spheres. In addition, compared with the loading of Pt particles, loading of 1D Pt nanowires on Ag_3PO_4 rhombic dodecahedrons separated and transferred photo-induced electrons more efficiently, resulting in the generation of more holes for RhB degradation. Thus, Pt nanowire-anchored dodecahedral Ag_3PO_4 achieved a much higher photocatalytic activity than Pt particles/dodecahedral Ag_3PO_4 . The concentration of pollutants was not changed during the photolysis test, while more than 98% of RhB was photodegraded over Pt nanowire-anchored dodecahedral Ag_3PO_4 within 12 min (Figure 4A). The degradation kinetics of RhB in this experiment can be well described by the pseudo-first-order kinetic model (Figure 4B). The rate constant of Pt nanowire-anchored dodecahedral Ag_3PO_4 (0.334 min^{-1}) was 1.67 times higher than that of irregular spherical Ag_3PO_4 (0.125 min^{-1}). In addition, the content of Pt nanowires showed an obvious influence on the photocatalytic activity. In the experiment range (0.2 wt%, 0.5 wt%, 1 wt%, 2 wt%), 0.5 wt% of Pt nanowire-anchored dodecahedral Ag_3PO_4 {110} exhibited the highest degradation rate of RhB (Figure 4C,D). The UV-vis absorption spectra (inset of Figure 4D) of RhB showed that RhB was completely degraded over 0.5 wt% Pt nanowire-anchored dodecahedral Ag_3PO_4 within 10 min. In order to comprehensively evaluate the visible-light photocatalytic activity of the samples, a photocatalytic degradation tests of bisphenol A (BPA) was conducted. As a result, BPA and its intermediates could also be photodegraded efficiently over 0.5 wt% Pt nanowire-anchored dodecahedral Ag_3PO_4 {110}, resulting in 80% removal rate of total organic carbon (TOC) (Figure S6). Further studies indicated that an increase of the light intensity, catalyst dosage, and pollutant concentration could improve the degradation kinetics (Table S1). However, an excessive loading of Pt nanowires on dodecahedral Ag_3PO_4 could cover the active facets (Figure S3), decreasing the photocatalytic activity.

Successive photocatalytic degradation of RhB was conducted to evaluate the anticorrosion ability of different samples. As expected, Pt nanowire-anchored dodecahedral Ag_3PO_4 exhibited excellent anti-photocorrosion ability. The degradation rate of RhB was high (>90%) even after 10 cycle runs, while other photocatalysts were seriously photo-corroded only after 3 cycle runs (Figure 5A). In addition, the color and morphology of Pt nanowire-anchored dodecahedral Ag_3PO_4 were not obviously changed after 10 cycles (Figure 5B). The XPS characteristic peaks (Ag 3d) and XRD patterns of Pt nanowire-anchored dodecahedral Ag_3PO_4 remained nearly unchanged after the reaction (Figure 5C,D), suggesting that Ag^+ was not reduced to Ag^0 [13]. Regarding the other samples, as shown by the changes of color and morphology, the XPS characteristic peaks of Ag 3d shifted with the appearance of the XRD diffraction peaks of silver (38.1° and 64.4°) (JCPDS NO.04-0783) (Figure 5C,D), indicating serious photocorrosion of Ag_3PO_4 during the reaction. Thus, loading Pt nanowires on Ag_3PO_4 can significantly enhance its anti-photocorrosion.

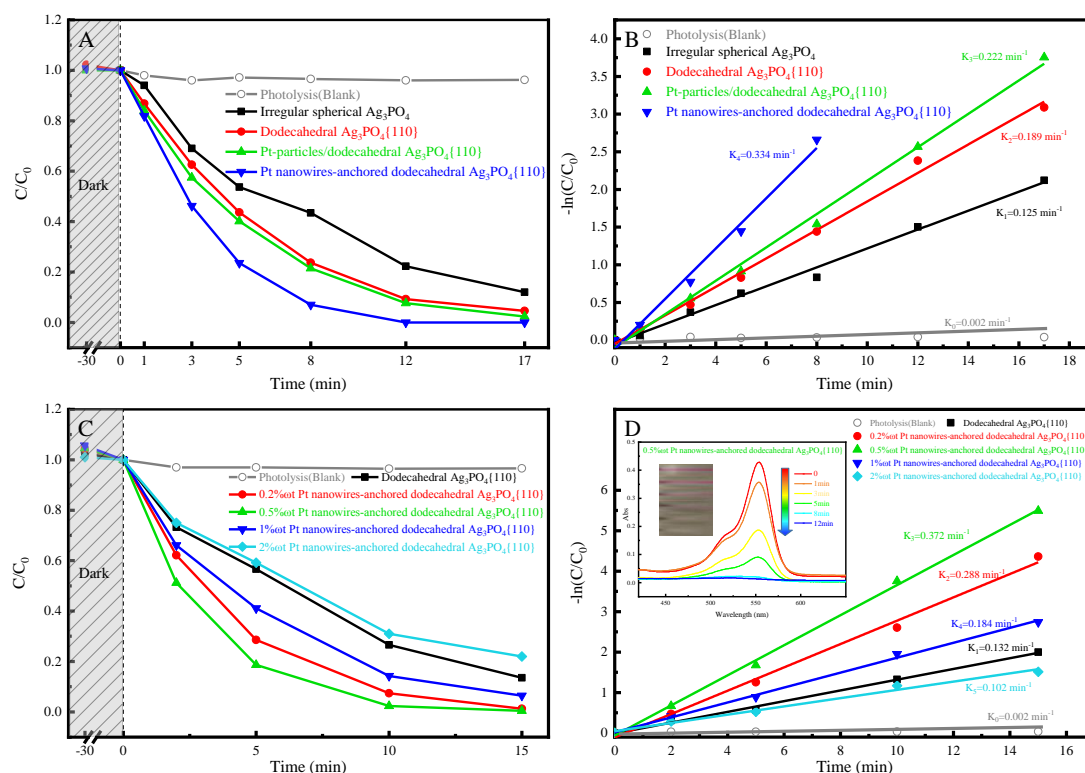


Figure 4. (A) Photolysis and photocatalytic degradation curves of Rhodamine B (RhB) over irregular spherical Ag_3PO_4 , dodecahedral $\text{Ag}_3\text{PO}_4\{110\}$, Pt particles/dodecahedral $\text{Ag}_3\text{PO}_4\{110\}$, and Pt nanowire-anchored dodecahedral $\text{Ag}_3\text{PO}_4\{110\}$, (B) their corresponding kinetic fitting curves, (C) photocatalytic degradation curves of RhB over 0.2 wt%, 0.5 wt%, 1 wt%, and 2 wt% Pt nanowire-anchored dodecahedral $\text{Ag}_3\text{PO}_4\{110\}$, and (D) their corresponding kinetic fitting curves. The inset of Figure 4D shows the UV-vis absorption spectra of the reaction solution during the degradation process of RhB over 0.5 wt% Pt nanowire-anchored dodecahedral $\text{Ag}_3\text{PO}_4\{110\}$.

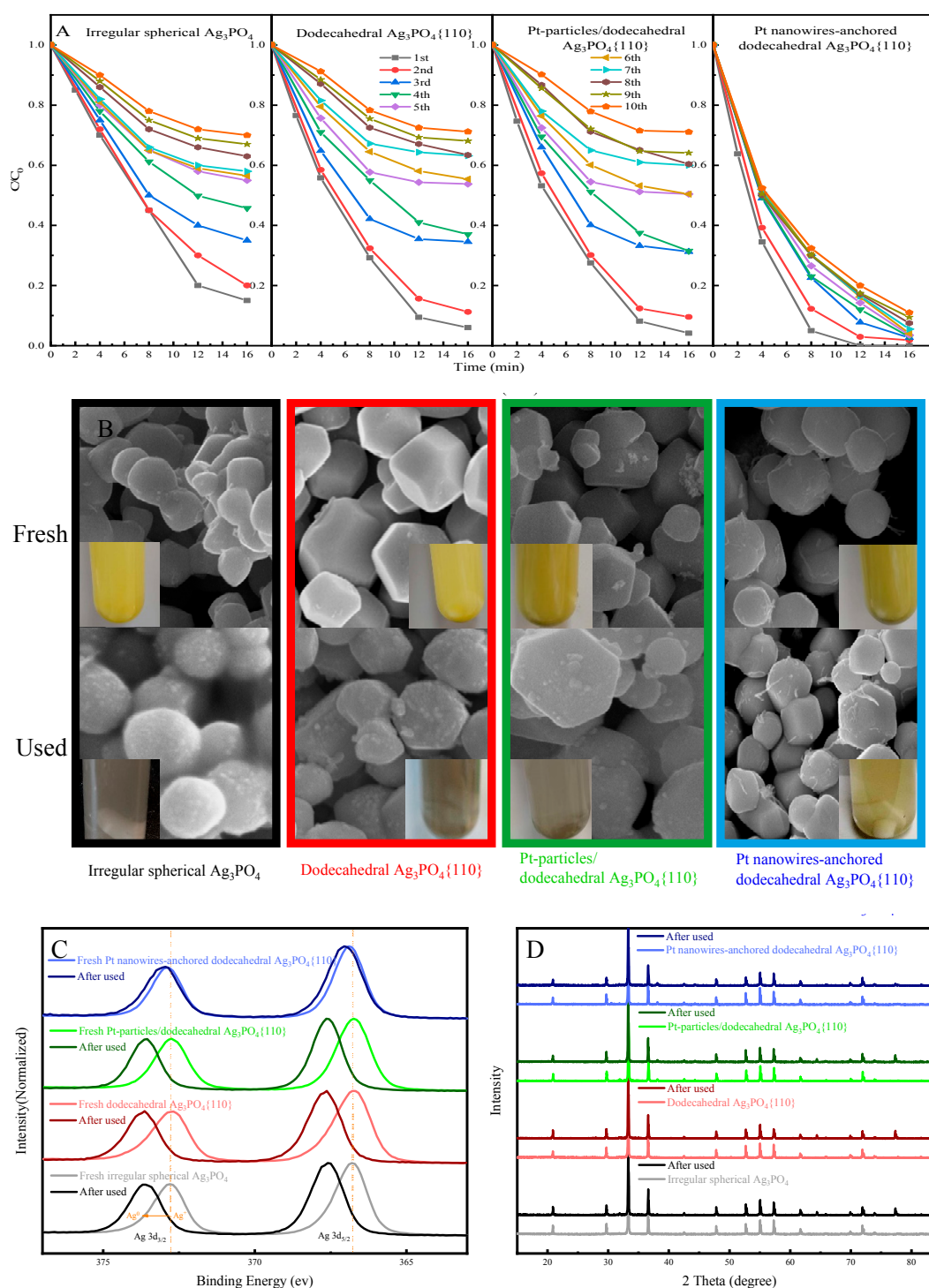


Figure 5. (A) Cycling runs of the photocatalytic degradation rate of RhB over different photocatalysts. (B) SEM images, (C) XPS spectra, and (D) XRD patterns of photocatalysts before and after the reaction.

2.4. Photocatalytic Mechanism

To further investigate the photocatalytic mechanism of Pt nanowire-anchored dodecahedral Ag_3PO_4 , free-radical trapping experiments and EPR analysis were conducted. As shown in Figure 6A, RhB degradation was not inhibited in the presence of TBA ($\cdot\text{OH}$ radical scavenger) but obviously decreased in the presence of EDTA (h^+ scavenger). Thus, h^+ , rather than the $\cdot\text{OH}$ radicals, played a dominant role in the photocatalytic degradation process. Interestingly, the addition of p-BQ ($\cdot\text{O}_2^-$

radical scavenger) showed more adverse effects on Pt nanowire-anchored dodecahedral Ag_3PO_4 than on pure dodecahedral Ag_3PO_4 , which indicated that loading Pt nanowires on Ag_3PO_4 could facilitate the production of $\cdot\text{O}_2^-$.

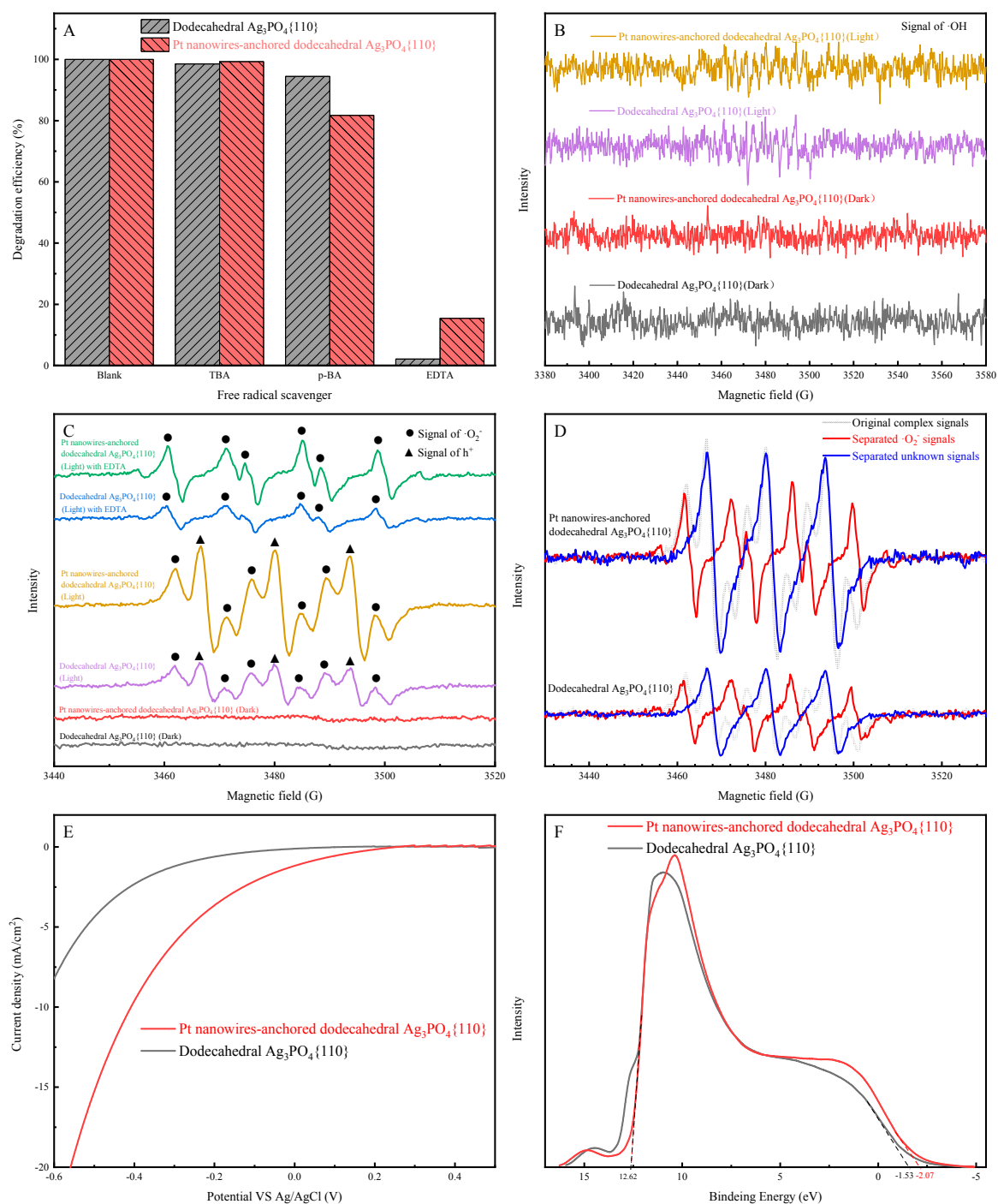


Figure 6. (A) Degradation rate of RhB in the presence of tert-butanol (TBA). Electron paramagnetic resonance (EPR) analysis of $\cdot\text{OH}$ (B) and $\cdot\text{O}_2^-$ (C), (D) fitting deconvoluted peaks of the detected $\cdot\text{O}_2^-$ signals over different photocatalysts, (E) electrochemical reduction curve of O_2 (with illumination) over pure dodecahedral Ag_3PO_4 and Pt nanowire-anchored dodecahedral Ag_3PO_4 , (F) Ultraviolet photoelectron spectrometer (UPS) of pure dodecahedral Ag_3PO_4 and Pt nanowire-anchored dodecahedral Ag_3PO_4 .

Signals of $\cdot\text{O}_2^-$ radicals were detected in the EPR analysis, while $\cdot\text{OH}$ radicals were not detected (Figure 6B), which is consistent with the trapping experiment results. Unexpectedly, some unknown peaks appeared with the $\cdot\text{O}_2^-$ peaks (Figure 6C). In order to identify these unknown peaks, EDTA (h^+ scavenger) was added in the detection system. Interestingly, $\cdot\text{O}_2^-$ radicals were still detected, while those unknown peaks disappeared in the presence of EDTA, suggesting that the unknown peaks might be ascribed to h^+ or its derivatives. As shown in the deconvolution of EPR spectra (Figure 6D), more h^+ and $\cdot\text{O}_2^-$ radicals were generated over Pt nanowire-anchored dodecahedral Ag_3PO_4 for organics degradation compared with pure dodecahedral Ag_3PO_4 . This could be explained as follows: 1D Pt nanowires could act as an electron sink, which promoted the separation of the charge carriers of Ag_3PO_4 because of the formation of the Schottky barrier. Meanwhile, due to their unique 1D structure, the Pt nanowires could not only facilitate the transfer of the separated electrons along the axial direction but also prolong the lifetime of the photogenerated carriers via long-distance transport and diffusion, resulting in the accumulation of large amounts of holes on the surface of dodecahedral Ag_3PO_4 and plenty of photogenerated electrons on the Pt nanowires. Furthermore, as the best catalysts for ORR, Pt nanowires could subsequently catalyze the reduction of O_2 to $\cdot\text{O}_2^-$ by these photogenerated electrons.

Photoelectrochemical reduction of O_2 was conducted to evaluate the oxygen reduction ability of the photogenerated electrons (Figure 6E). Compared with pure dodecahedral Ag_3PO_4 , Pt nanowire-anchored dodecahedral Ag_3PO_4 showed a more positive onset potential, suggesting a higher reduction current of O_2 under the same voltage [41]. Thus, Pt nanowires loaded on dodecahedral Ag_3PO_4 can obviously enhance the utilization of photo-induced electrons for oxygen reduction. In the present work, the structure of the energy bands of the photocatalyst was analyzed by Ultraviolet photoelectron spectrometer (UPS) spectra (Figure 6F). By using the linear intersection method [42,43], the maximum valence bands of Ag_3PO_4 and Pt nanowire-anchored dodecahedral Ag_3PO_4 were estimated to be -7.07 eV and -6.53 eV (vs. vacuum), respectively. According to the equations $E_g = E_{\text{VB}} - E_{\text{CB}}$, and $E_{\text{V}} = -E_{\text{NHE}} - 4.44$ eV, the $E_{\text{CB}}/E_{\text{VB}}$ (vs. NHE) of pure dodecahedral Ag_3PO_4 and Pt nanowire-anchored dodecahedral Ag_3PO_4 were calculated to be $+0.21/+2.63$ eV and $-0.26/+2.09$ eV (vs. NHE), respectively. Notably, the loading of Pt nanowires could obviously decrease the CB and VB of Ag_3PO_4 , which significantly improved the reduction potential of photo-induced electrons. Such conclusions are well consistent with the result of the photoelectrochemical reduction of O_2 (Figure 6E). Thus, the photogenerated electrons of Pt nanowire-anchored dodecahedral Ag_3PO_4 could be efficiently utilized for O_2 reduction ($\text{O}_2 + \text{e}^- \rightarrow \cdot\text{O}_2^-$, $\text{O}_2 + 4 \text{e}^- + 4 \text{H}^+ \rightarrow 2 \text{H}_2\text{O}$), preventing the photocorrosion of Ag_3PO_4 .

Based on the above research, the possible photocatalytic mechanism of Pt nanowire-anchored dodecahedral $\text{Ag}_3\text{PO}_4\{110\}$ can be elucidated (Figure 7). Under visible-light irradiation, rhombic dodecahedral Ag_3PO_4 , which is entirely bounded by $\{110\}$ facets, could achieve a much higher photocatalytic activity than common Ag_3PO_4 crystals. Furthermore, 1D Pt nanowires loaded on the surface of dodecahedral Ag_3PO_4 could not only improve the separation of the charge carriers due to the Schottky barrier but also provide a fast transfer of the photogenerated electrons in the axial direction. Such long-distance transport and diffusion on 1D Pt nanowires could efficiently prolong the photogenerated carriers' lifetime. Thus, large amounts of holes were accumulated on the surface of dodecahedral Ag_3PO_4 for organics degradation. On the other hand, as the best catalyst for ORR, Pt nanowires could significantly improve the reduction potential of the photogenerated electrons by CB bending, as a result of the Schottky barrier, which facilitated the utilization of the photogenerated electrons for oxygen reduction. Such utilization of the photogenerated electrons for oxygen reduction could not only fundamentally resolve the problem of Ag_3PO_4 photocorrosion but also provide $\cdot\text{O}_2^-$ for organics degradation.

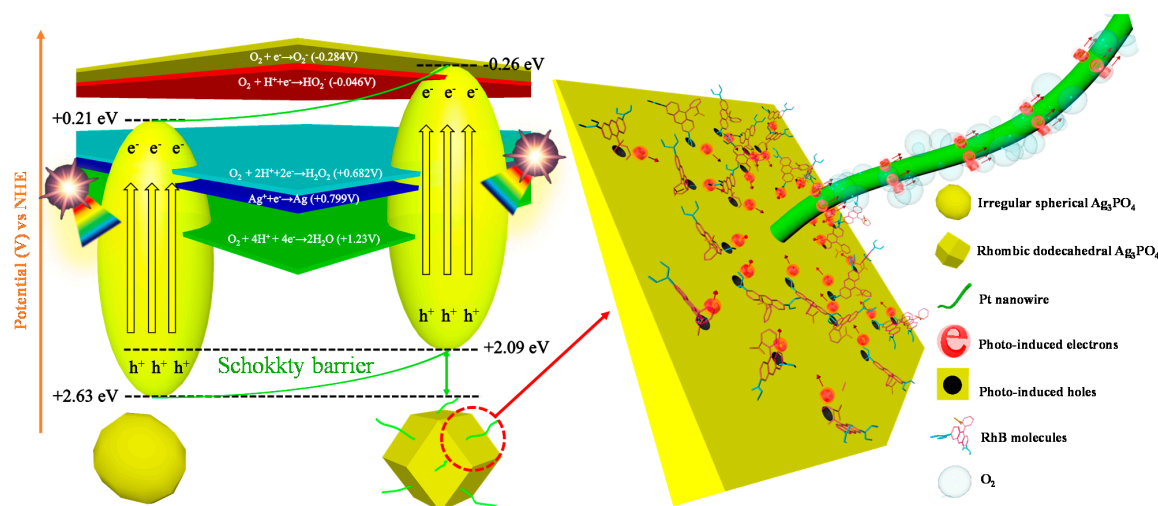


Figure 7. Photocatalytic mechanism of Pt nanowire-anchored dodecahedral $\text{Ag}_3\text{PO}_4\{110\}$.

3. Materials and Methods

3.1. Chemicals

Chloroplatinic acid hexahydrate ($\text{H}_2\text{PtCl}_6 \cdot 6\text{H}_2\text{O}$), potassium hydroxide (KOH), silver nitrate (AgNO_3), silver acetate (CH_3COOAg) were ordered from National Medicines Corporation Ltd. of China. Dibasic sodium phosphate (Na_2HPO_4), ethylene glycol (EG), N, N-dimethylmethanamide (DMF), acetic acid (CH_3COOH), formaldehyde (HCHO), ethylenediaminetetraacetic acid (EDTA), tert-butanol (TBA), p-benzoquinone (p-BQ), were supplied by Aladdin Industrial Corporation of China. All the chemicals used in this work were analytical-grade and were used without further purification.

3.2. Synthesis of Pt Nanowire-Anchored Dodecahedral $\text{Ag}_3\text{PO}_4\{110\}$

Synthesis of single Pt nanowires: In a typical synthesis, 0.4 mL of 50 mM H_2PtCl_6 solution and 0.7 g of potassium hydroxide were added to a mixture of EG (5 mL) and DMF (5 mL). After magnetic stirring for 2 h, the mixture was transferred into a 25 mL Teflon-lined autoclave. The autoclave was kept at 170 °C for 8 h and then cooled to room temperature. The obtained Pt nanowire nets were collected after washed with ethanol and deionized water (DI) and dried at 80 °C for 5 h. Then, the products were broken into single nanowires by using an ultrasonic cell disruptor homogenizer. Finally, a black homogeneous suspension of Pt single nanowires with the obvious Tyndall effect could be obtained. Moreover, the Pt particles were synthesized as referenced by the addition of 1 mL of HCHO into 0.4 mL of a 50 mM H_2PtCl_6 solution.

Synthesis of uniform Ag_3PO_4 rhombic dodecahedrons: Typically, 0.2 g of CH_3COOAg was dissolved in 50 mL DI water in a beaker using ultrasounds for 3 h. Then, 0.4 mL of pure CH_3COOH liquid was added into the above solution and mixed completely. At this point, a 0.15 M Na_2HPO_4 solution was slowly dropped into the mixture under vigorous stirring to obtain a yellow suspension of Ag_3PO_4 . After stirring and stabilizing the mixture in the dark for 30 min, the resulting yellow samples were collected. Then, the samples were washed and dried. Irregular spherical Ag_3PO_4 was synthesized by the same method, except that AgNO_3 was used as the precursor instead of CH_3COOAg .

Synthesis of Pt nanowire-anchored dodecahedral $\text{Ag}_3\text{PO}_4\{110\}$: A certain amount of the homogeneous suspension of Pt single nanowires was added into 50 mL of a CH_3COOAg solution. Then, CH_3COOH and Na_2HPO_4 were dropped into the mixture under vigorous stirring to obtain Pt nanowire-anchored dodecahedral $\text{Ag}_3\text{PO}_4\{110\}$. In addition, Pt particles/dodecahedral $\text{Ag}_3\text{PO}_4\{110\}$ was synthesized by the same method, except that a suspension of Pt particles was used instead of a Pt single-nanowire suspension.

3.3. Characterization of the Catalysts

The morphology of the catalysts was characterized by environmental scanning electron microscopy (FEG ESEM, QUANTA250, FEI, Hillsboro, USA) and transmission electron microscopy (TEM, JEM-200CX, JEOL, (Tokyo, Japan). Surface element chemical analysis of the samples was carried out by X-ray photoelectron spectroscopy (XPS, PHI5000 Versa Probe III, ULVAC-PHI, Chigasaki, Japan) with an Al- k_{α} X-ray source of 1486.6 eV. The conduction band energy of the photocatalysts was also determined by XPS with a He I UV-light source of 21.22 eV. The binding energies in the XPS spectra were referenced to the C 1s peak at 284.8 eV. The XRD patterns were obtained on an X-ray diffractometer (XRD, X'TRA, Switzerland) using Cu- k_{α} radiation at a scan rate of 5°/min in the range of 10–80° (2 θ). The EIS (electrochemical impedance spectroscopy) and photocurrent responses of the photocatalysts under illumination (350 W xenon lamp) were measured by an electrochemical workstation (CHI660E, Chenhua, Shanghai, China) with a conventional three-electrode system composed of a counter electrode of Pt wire and a reference electrode of Ag/AgCl. The UV–vis diffuse reflectance spectra (UV–visDRS) were obtained with a UV–vis spectrophotometer (UV-2600, Shimadzu, Kyoto, Japan) with an integrating sphere. The photoluminescence (PL) spectra of the photocatalysts were detected by fluorescence spectrometry (FM4P-TCSPC, Horiba, Kyoto, Japan).

3.4. Photocatalytic Tests of the Catalysts

To comparatively study the photocatalytic performances of the different as-prepared photocatalysts, typically, 15 mg of a photocatalyst was added into an RhB (Rhodamine B) aqueous solution (5 mg/L, 50 mL) in the XPA-photochemical reactor (Xujiang Electrochemical Plant, Nanjing, China), and the mixture was stirred in the dark for 30 min. The temperature of the reactor was monitored by a thermometer and maintained at 25 ± 2 °C by a water bath circulating system. Then, under the irradiation of a 350 W xenon (Xe) lamp (with a cut-off filter, $\lambda > 420$ nm), 3 mL samples of the suspension were collected at given time intervals and then centrifuged at 3700 rpm for 5 min. The concentration of RhB was determined by its characteristic optical absorption at 554 nm with a UV–vis spectrophotometer (UV-1800, Shimadzu, Japan). In addition, successive cycles of photocatalytic degradation of RhB were conducted to evaluate the photocatalytic stability.

3.5. Photocatalytic Mechanism of Pt Nanowire-Anchored Dodecahedral Ag₃PO₄{110}

The active species generated in the photocatalytic system could be measured by adding EDTA (5 mM), TBA (5 mM), and p-BQ (5 mM) before the photodegradation reaction, as an h⁺ radical scavenger, an ·OH radical scavenger, and an ·O₂[−] radical scavenger, respectively. All of the photodegradation conditions were the same as mentioned above. To further precisely analyze the radicals of the photocatalytic reaction, electron paramagnetic resonance (EPR) spectra of the photocatalyst were recorded on EMX-10/12 (Bruker, Germany) with a 350 W xenon (Xe) lamp (with a cut-off filter, $\lambda > 420$ nm) at room temperature, in which 5, 5-dimethyl-1-pyrroline-N-oxide (DMPO) was used as the spin trap. The electrochemical reduction curve of O₂ was measured by the electrochemical workstation (CHI660E, Chenhua, Shanghai, China) with 350 W Xe lamp illumination and high-purity O₂ gas bubbled in the electrolyte (0.5 M Na₂SO₄) continuously.

4. Conclusions

In the present work, we successfully constructed Pt nanowire-anchored dodecahedral Ag₃PO₄{110} with high photocatalytic activity and anti-photocorrosion properties for organics degradation. Being entirely bounded by {110} facets, dodecahedral Ag₃PO₄ achieved a much higher photocatalytic activity than other types of Ag₃PO₄ crystals. We found that 1D Pt nanowires loaded on dodecahedral Ag₃PO₄ obviously improved the separation of the charge carriers because of the formation of a Schottky barrier. Meanwhile, 1D Pt nanowires not only provided a fast transfer of the photogenerated electrons but also prolonged the lifetime of the charge carriers, resulting in the accumulation

of holes for organics degradation. On the other hand, Pt nanowires significantly enhanced the reduction potential of the photogenerated electrons for oxygen reduction, which efficiently improved the anti-photocorrosion of Ag_3PO_4 . Thus, this work provides a new method to enhance the anti-photocorrosion of Ag_3PO_4 -based photocatalysts by simultaneously promoting spatial charge separation and photogenerated electron utilization.

Supplementary Materials: The following are available online at <http://www.mdpi.com/2073-4344/10/2/206/s1>, Figure S1: SEM images of obtained pure Ag_3PO_4 with the addition of different amount of acetic acid in the synthesis experiment: (A) 0mL, (B) 0.1mL, (C) 0.2mL, (D) 0.4mL, Figure S2: SEM images of synthesized (A) Pt nanowires assemblies and the stripped products by ultrasonic exfoliation for (B) 5h and (C) 10h, Figure S3: SEM images of synthesized Pt nanowires-anchored dodecahedral $\text{Ag}_3\text{PO}_4\{110\}$ with different amount of Pt nanowires: (A) 0.2 wt%, (B) 0.5 wt%, (C) 1 wt%, (D) 2 wt%. Figure S4: FT-IR spectrum of as-prepared Pt nanowires. Figure S5: The high resolution XPS spectrum for (A) P 2p, (B) O 1s, (C) Ag 3d of pure Ag_3PO_4 and Pt-nanowires/ Ag_3PO_4 composite. Figure S6: Photolysis curves and photocatalytic degradation curves (A) of bisphenol A and the corresponding TOC removal curves over 2 wt% Pt nanowires-anchored dodecahedral $\text{Ag}_3\text{PO}_4\{110\}$; (B) the concentration variation curves of BPA and its intermediate product in the degradation process, Table S1: Photocatalytic degradation of RhB over Ag_3PO_4 -based photocatalysts in previous literatures and this work.

Author Contributions: H.Z. and J.W. conceived this study; H.Z., Y.J., L.C. and W.B. equally contributed to the design and performed the experiments as well as analyzed the data; H.Z. wrote the paper. All authors have read and agreed to the published version of the manuscript.

Funding: This research was funded by the National Natural Science Foundation of China (No. 51878335). And the APC was funded by the National major science and technology program for water pollution control and management (No. 2018ZX07402005-04).

Acknowledgments: The author thanked the Water Resource Research Project of Jiangsu Province (2017043) and the Natural Science Foundation of Jiangsu province (BK20191255).

Conflicts of Interest: The authors declare no conflicts of interest.

References

1. Martin, D.J.; Liu, G.; Moniz, S.J.; Bi, Y.; Beale, A.M.; Ye, J.; Tang, J. Efficient visible driven photocatalyst, silver phosphate: performance, understanding and perspective. *Chem. Soc. Rev.* **2015**, *44*, 7808–7828. [[CrossRef](#)]
2. Yi, Z.; Ye, J.; Kikugawa, N.; Kako, T.; Ouyang, S.; Stuart-Williams, H.; Yang, H.; Cao, J.; Luo, W.; Li, Z.; et al. An orthophosphate semiconductor with photooxidation properties under visible-light irradiation. *Nat. Mater.* **2010**, *9*, 559–564. [[CrossRef](#)]
3. Liu, G.; Jimmy, C.Y.; Lu, G.Q.M.; Cheng, H.M. Crystal facet engineering of semiconductor photocatalysts: motivations, advances and unique properties. *Chem. Comm.* **2011**, *47*, 6763–6783. [[CrossRef](#)]
4. Bai, S.; Wang, L.; Li, Z.; Xiong, Y. Facet-Engineered Surface and Interface Design of Photocatalytic Materials. *Adv. Sci.* **2017**, *4*, 1600216. [[CrossRef](#)] [[PubMed](#)]
5. Bi, Y.; Ouyang, S.; Umezawa, N.; Cao, J.; Ye, J. Facet effect of single-crystalline Ag_3PO_4 sub-microcrystals on photocatalytic properties. *J. Am. Chem. Soc.* **2011**, *133*, 6490–6492. [[CrossRef](#)]
6. Martin, D.J.; Umezawa, N.; Chen, X.; Ye, J.; Tang, J. Facet engineered Ag_3PO_4 for efficient water photooxidation. *Energy Environ. Sci.* **2013**, *6*, 3380. [[CrossRef](#)]
7. Liang, Q.; Ma, W.; Shi, Y.; Li, Z.; Yang, X. Hierarchical Ag_3PO_4 porous microcubes with enhanced photocatalytic properties synthesized with the assistance of trisodium citrate. *CrystEngComm* **2012**, *14*, 2966. [[CrossRef](#)]
8. Li, X.-Z.; Wu, K.-L.; Dong, C.; Xia, S.-H.; Ye, Y.; Wei, X.-W. Size-controlled synthesis of Ag_3PO_4 nanorods and their high-performance photocatalysis for dye degradation under visible-light irradiation. *Mater. Lett.* **2014**, *130*, 97–100. [[CrossRef](#)]
9. Wang, H.; He, L.; Wang, L.; Hu, P.; Guo, L.; Han, X.; Li, J. Facile synthesis of Ag_3PO_4 tetrapod microcrystals with an increased percentage of exposed {110} facets and highly efficient photocatalytic properties. *CrystEngComm* **2012**, *14*, 8342–8344. [[CrossRef](#)]
10. Dong, P.; Wang, Y.; Li, H.; Li, H.; Ma, X.; Han, L. Shape-controllable synthesis and morphology-dependent photocatalytic properties of Ag_3PO_4 crystals. *J. Mater. Chem. A* **2013**, *1*, 4651. [[CrossRef](#)]
11. Guo, R.; Fan, Y.; Tang, Y. Interesting Ag_3PO_4 concave rhombic dodecahedra: the same face with different morphologies and photocatalytic properties. *RSC Adv.* **2017**, *7*, 23977–23981. [[CrossRef](#)]

12. Shao, N.; Hou, Z.; Zhu, H.; Wang, J.; François-Xavier, C.P. Novel 3D core-shell structured CQDs/Ag₃PO₄@Benzoxazinetetrapods for enhancement of visible-light photocatalytic activity and anti-photocorrosion. *Appl. Catal. B: Environ.* **2018**, *232*, 574–586. [[CrossRef](#)]
13. Cai, T.; Wang, L.; Liu, Y.; Zhang, S.; Dong, W.; Chen, H.; Yi, X.; Yuan, J.; Xia, X.; Liu, C., et al. Ag₃PO₄/Ti₃C₂ MXene interface materials as a Schottky catalyst with enhanced photocatalytic activities and anti-photocorrosion performance. *Appl. Catal. B: Environ.* **2018**, *239*, 545–554. [[CrossRef](#)]
14. Tan, P.; Chen, X.; Wu, L.; Shang, Y.Y.; Liu, W.; Pan, J.; Xiong, X. Hierarchical flower-like SnSe₂ supported Ag₃PO₄ nanoparticles: Towards visible light driven photocatalyst with enhanced performance. *Appl. Catal. B: Environ.* **2017**, *202*, 326–334. [[CrossRef](#)]
15. Tang, C.; Liu, E.; Wan, J.; Hu, X.; Fan, J. Co₃O₄ nanoparticles decorated Ag₃PO₄ tetrapods as an efficient visible-light-driven heterojunction photocatalyst. *Appl. Catal. B: Environ.* **2016**, *181*, 707–715. [[CrossRef](#)]
16. Shi, W.; Guo, F.; Yuan, S. In situ synthesis of Z-scheme Ag₃PO₄/CuBi₂O₄ photocatalysts and enhanced photocatalytic performance for the degradation of tetracycline under visible light irradiation. *Appl. Catal. B: Environ.* **2017**, *209*, 720–728. [[CrossRef](#)]
17. Yang, X.; Tian, L.; Zhao, X.; Tang, H.; Liu, Q.; Li, G. Interfacial optimization of g-C₃N₄-based Z-scheme heterojunction toward synergistic enhancement of solar-driven photocatalytic oxygen evolution. *Appl. Catal. B: Environ.* **2019**, *244*, 240–249. [[CrossRef](#)]
18. Zhang, C.; Yu, K.; Feng, Y.; Chang, Y.; Yang, T.; Xuan, Y.; Lei, D.; Lou, L.-L.; Liu, S. Novel 3DOM-SrTiO₃/Ag/Ag₃PO₄ ternary Z-scheme photocatalysts with remarkably improved activity and durability for contaminant degradation. *Appl. Catal. B: Environ.* **2017**, *210*, 77–87. [[CrossRef](#)]
19. Shao, N.; Wang, J.; Wang, D.; Corvini, P. Preparation of three-dimensional Ag₃PO₄/TiO₂@MoS₂ for enhanced visible-light photocatalytic activity and anti-photocorrosion. *Appl. Catal. B: Environ.* **2017**, *203*, 964–978. [[CrossRef](#)]
20. Cai, T.; Liu, Y.; Wang, L.; Zhang, S.; Zeng, Y.; Yuan, J.; Ma, J.; Dong, W.; Liu, C.; Luo, S. Silver phosphate-based Z-Scheme photocatalytic system with superior sunlight photocatalytic activities and anti-photocorrosion performance. *Appl. Catal. B: Environ.* **2017**, *208*, 1–13. [[CrossRef](#)]
21. Wang, H.; Zhang, L.; Chen, Z.; Hu, J.; Li, S.; Wang, Z.; Liu, J.; Wang, X. Semiconductor heterojunction photocatalysts: design, construction, and photocatalytic performances. *Chem. Soc. Rev.* **2014**, *43*, 5234–5244. [[CrossRef](#)] [[PubMed](#)]
22. Liu, X.; Iocozzia, J.; Wang, Y.; Cui, X.; Chen, Y.; Zhao, S.; Li, Z.; Lin, Z. Noble metal–metal oxide nanohybrids with tailored nanostructures for efficient solar energy conversion, photocatalysis and environmental remediation. *Energy Environ. Sci.* **2017**, *10*, 402–434. [[CrossRef](#)]
23. Li, G.; Tang, Z. Noble metal nanoparticle@metal oxide core/yolk-shell nanostructures as catalysts: Recent progress and perspective. *Nanoscale* **2014**, *6*, 3995–4011. [[CrossRef](#)] [[PubMed](#)]
24. Bora, T.; Kyaw, H.H.; Sarkar, S.; Pal, S.K.; Dutta, J. Highly efficient ZnO/Au Schottky barrier dye-sensitized solar cells: Role of gold nanoparticles on the charge-transfer process. *Beilstein J. Nanotechnol.* **2011**, *2*, 681–690. [[CrossRef](#)] [[PubMed](#)]
25. Hou, Z.; Chen, F.; Wang, J.; François-Xavier, C.P.; Wintgens, T. Novel Pd/GdCrO₃ composite for photo-catalytic reduction of nitrate to N₂ with high selectivity and activity. *Appl. Catal. B: Environ.* **2018**, *232*, 124–134. [[CrossRef](#)]
26. Khan, M.R.; Chuan, T.W.; Yousuf, A.; Chowdhury, M.N.K.; Cheng, C.K. Schottky barrier and surface plasmonic resonance phenomena towards the photocatalytic reaction: Study of their mechanisms to enhance photocatalytic activity. *Catal. Sci. Technol.* **2015**, *5*, 2522–2531. [[CrossRef](#)]
27. Cademartiri, L.; Ozin, G.A. Ultrathin nanowires - A materials chemistry perspective. *Adv. Mater.* **2009**, *21*, 1013–1020. [[CrossRef](#)]
28. Teng, X.; Han, W.Q.; Ku, W.; Hücker, M. Synthesis of ultrathin palladium and platinum nanowires and a study of their magnetic properties. *Angew. Chem.* **2008**, *120*, 2085–2088. [[CrossRef](#)]
29. Wang, W.; Lv, F.; Lei, B.; Wan, S.; Luo, M.; Guo, S. Tuning Nanowires and Nanotubes for Efficient Fuel-Cell Electrocatalysis. *Adv. Mater.* **2016**, *28*, 10117–10141. [[CrossRef](#)]
30. Liu, S.; Tang, Z.R.; Sun, Y.; Colmenares, J.C.; Xu, Y.J. One-dimension-based spatially ordered architectures for solar energy conversion. *Chem. Soc. Rev.* **2015**, *44*, 5053–5075. [[CrossRef](#)]

31. Abe, R.; Takami, H.; Murakami, N.; Ohtani, B. Pristine simple oxides as visible light driven photocatalysts: Highly efficient decomposition of organic compounds over platinum-loaded tungsten oxide. *J. Am. Chem. Soc.* **2008**, *130*, 7780–7781. [[CrossRef](#)] [[PubMed](#)]
32. Nie, Y.; Li, L.; Wei, Z. Recent advancements in Pt and Pt-free catalysts for oxygen reduction reaction. *Chem. Soc. Rev.* **2015**, *44*, 2168–2201. [[CrossRef](#)] [[PubMed](#)]
33. Shao, Q.; Li, F.; Chen, Y.; Huang, X. The Advanced Designs of High-Performance Platinum-Based Electrocatalysts: Recent Progresses and Challenges. *Adv. Mater. Interfaces* **2018**, *5*, 5. [[CrossRef](#)]
34. Nørskov, J.K.; Rossmeisl, J.; Logadottir, A.; Lindqvist, L.; Kitchin, J.R.; Bligaard, T.; Jónsson, H. Origin of the overpotential for oxygen reduction at a fuel-cell cathode. *J. Phys. Chem. B* **2004**, *108*, 17886–17892. [[CrossRef](#)]
35. Kitchin, J.R.; Nørskov, J.K.; Barteau, M.A.; Chen, J.G. Modification of the surface electronic and chemical properties of Pt(111) by subsurface 3d transition metals. *J. Chem. Phys.* **2004**, *120*, 10240–10246. [[CrossRef](#)]
36. Xia, B.Y.; Wu, H.B.; Yan, Y.; Lou, X.W.; Wang, X. Ultrathin and ultralong single-crystal platinum nanowire assemblies with highly stable electrocatalytic activity. *J. Am. Chem. Soc.* **2013**, *135*, 9480–9485. [[CrossRef](#)]
37. Yin, H.; Zhao, S.; Zhao, K.; Muqsit, A.; Tang, H.; Chang, L.; Zhao, H.; Gao, Y.; Tang, Z. Ultrathin platinum nanowires grown on single-layered nickel hydroxide with high hydrogen evolution activity. *Nat. Commun.* **2015**, *6*, 6430. [[CrossRef](#)]
38. Miao, X.; Yue, X.; Ji, Z.; Shen, X.; Zhou, H.; Liu, M.; Xu, K.; Zhu, J.; Zhu, G.; Kong, L., et al. Nitrogen-doped carbon dots decorated on g-C₃N₄/Ag₃PO₄ photocatalyst with improved visible light photocatalytic activity and mechanism insight. *Appl. Catal. B: Environ.* **2018**, *227*, 459–469. [[CrossRef](#)]
39. Ye, C.; Li, J.-X.; Li, Z.-J.; Li, X.-B.; Fan, X.-B.; Zhang, L.-P.; Chen, B.; Tung, C.-H.; Wu, L.-Z. Enhanced Driving Force and Charge Separation Efficiency of Protonated g-C₃N₄ for Photocatalytic O₂ Evolution. *ACS Catal.* **2015**, *5*, 6973–6979. [[CrossRef](#)]
40. Lin, R.; Wan, J.; Xiong, Y.; Wu, K.; Cheong, W.C.; Zhou, G.; Wang, D.; Peng, Q.; Chen, C.; Li, Y. Quantitative Study of Charge Carrier Dynamics in Well-Defined WO₃ Nanowires and Nanosheets: Insight into the Crystal Facet Effect in Photocatalysis. *J. Am. Chem. Soc.* **2018**, *140*, 9078–9082. [[CrossRef](#)]
41. Liu, C.; Jing, L.; He, L.; Luan, Y.; Li, C. Phosphate-modified graphitic C₃N₄ as efficient photocatalyst for degrading colorless pollutants by promoting O₂ adsorption. *Chem. Commun.* **2014**, *50*, 1999–2001. [[CrossRef](#)] [[PubMed](#)]
42. Yuan, L.; Weng, B.; Colmenares, J.C.; Sun, Y.; Xu, Y.J. Multichannel Charge Transfer and Mechanistic Insight in Metal Decorated 2D-2D Bi₂WO₆-TiO₂ Cascade with Enhanced Photocatalytic Performance. *Small* **2017**, *13*, 1702253. [[CrossRef](#)] [[PubMed](#)]
43. Yan, X.; Ohno, T.; Nishijima, K.; Abe, R.; Ohtani, B. Is methylene blue an appropriate substrate for a photocatalytic activity test? A study with visible-light responsive titania. *Chem. Phys. Lett.* **2006**, *429*, 606–610. [[CrossRef](#)]

